

A feedback-controlled optoelectronic platform for programming interactions in active matter

Shutong Guo(郭姝彤), Zhiqing Huang(黄芷晴), Bingrui Xu(徐冰睿), Shuailong Zhang(张帅龙), and H. P. Zhang(张何朋)

Citation: Chin. Phys. B, 2026, 35 (**7**): 070502. DOI: 10.1088/1674-1056/ae6320
http://cpb.iphy.ac.cn; http://iopscience.iop.org/cpb

What follows is a list of articles you may be interested in

Spiral trajectories of asymmetric molecules

Nan Sheng(盛楠), Shiqi Sheng(盛世奇), Yu-Song Tu(涂育松), Rong-Zheng Wan(万荣正), Zuo-Wei Wang(王作维), Zhanchun Tu(涂展春), and Hai-Ping Fang(方海平)

Chin. Phys. B, 2025, 34 (**8**): 080507. DOI: 10.1088/1674-1056/adcea0

Enhancing phase separation of double-chiral particles by regulating inter-chiral frustration

Yi-Chen Lu(陆羿辰), Wan-Rou Cai(蔡婉柔), Meng-Chu Wang(王梦楚), Ya-Li Liu(刘雅莉), Tong Zhu(朱童), Yi-Lin Zhou(周怡琳), Tian-Chen Yu(余天晨), Yun-Xuan Ji(纪蕴轩), Ming-Qian Ao(敖明茜), Chen-Lu Li(李晨璐), Cheng-Xu Yan(颜乘旭), and Zhi-Gang Zheng(郑志刚)

Chin. Phys. B, 2025, 34 (**8**): 080506. DOI: 10.1088/1674-1056/ade06f

Transition from isotropic to polar state of self-driven eccentric disks

Jinghan Wang(王静晗), Tianliang Xu(许天亮), Jingxi He(何景熙), Kang Chen(陈康), and Wende Tian(田文得)

Chin. Phys. B, 2023, 32 (**7**): 070501. DOI: 10.1088/1674-1056/accd4d

Evaluating physical changes of iron oxide nanoparticles due to surface modification with oleic acid

S Rosales, N Casillas, A Topete, O Cervantes, G Gonz\'alez, J A Paz, and M E Cano†

Chin. Phys. B, 2020, 29 (**10**): 100502. DOI: 10.1088/1674-1056/aba2dc

Symmetry properties of fluctuations in an actively driven rotor

He Li(李赫), Xiang Yang(杨翔), Hepeng Zhang(张何朋)

Chin. Phys. B, 2020, 29 (**6**): 060502. DOI: 10.1088/1674-1056/ab862b

---

RAPID COMMUNICATION

A feedback-controlled optoelectronic platform for programming interactions in active matter

Shutong Guo(郭姝彤)[1], Zhiqing Huang(黄芷晴)[1], Bingrui Xu(徐冰睿)[2], Shuailong Zhang(张帅龙)[3], and H. P. Zhang(张何朋)[1,†]

[1] *School of Physics and Astronomy, Institute of Natural Sciences and MOE-LSC, Shanghai Jiao Tong University, Shanghai* 200240, *China*
[2] *Beijing Advanced Innovation Center for Intelligent Robots and Systems, School of Mechatronical Engineering, Beijing Institute of Technology, Beijing* 100081, *China*
[3] *School of Integrated Circuits and Electronics, Beijing Institute of Technology, Beijing* 100081, *China*

(Received 13 March 2026; revised manuscript received 12 April 2026; accepted manuscript online 22 April 2026)

Active matter systems involve complex interactions between constituent particles, often mediated by physical or chemical fields, and in some cases, governed by sensing or decision-making processes. Experimentally controlling such interactions remains highly challenging, posing a major obstacle to systematic investigation. In this work, we present an optoelectronic tweezer (OET) platform that uses closed-loop feedback to program both motion and interactions in colloidal systems by dynamically patterning local electric fields with light. Operating at very low optical intensities, this approach allows rapid and precise control over dielectrophoretic forces acting on colloidal particles. We demonstrate the capabilities of this platform through the experimental realization of both a programmable active Brownian particle system and a communicating active particle system. This versatile platform bridges theoretical models of active matter and their experimental realization, enabling direct control over propulsion and interaction rules.

Keywords: active matter, colloid, optoelectronic-tweezers, programmable interactions

PACS: 05.65.+b, 82.70.Dd, 42.50.Wk, 89.75.Fb

DOI: 10.1088/1674-1056/ae6320 **CSTR:** 32038.14.CPB.ae6320

1. Introduction

Active matter comprises self-driven units that convert locally stored or ambient free energy into mechanical motion, thereby sustaining persistent nonequilibrium states.[1–4] At the level of individual units, intrinsic activity continuously drives these systems out of thermal equilibrium and generates diverse forms of interaction. In artificial microswimmer systems, for example, colloidal particles interact through chemical, electrostatic, and hydrodynamic fields, leading to long-ranged and often non-reciprocal many-body interactions that violate Newton's third law.[5–11] Comparable complexity also emerges in biological collectives, where interactions are further shaped by sensing, information processing, and decision-making.[12,13] These diverse interaction mechanisms underpin a broad spectrum of collective behaviors, including flocking,[6,14] swarming,[15,16] clustering and motility-induced phase separation,[5,17] and synchronization.[18] These emergent phenomena further provide guiding principles for the design of adaptive and programmable materials.[1–4]

Active interactions mediated by complex physical fields or behavioral rules are generally difficult to control experimentally in conventional active-matter systems. To address this challenge, researchers have increasingly turned to artificial platforms based on macroscopic robots and microscopic active colloids, in which feedback control provides an additional degree of freedom for engineering effective interactions. These two classes of systems offer complementary routes toward programmable active matter.

At the macroscopic scale, robotic active-matter platforms provide precise agent-level control and flexible implementation of interaction rules, but they typically operate in an inertial regime that is physically distinct from the low-Reynolds-number environments relevant to colloidal and biological active matter.[19] Recent studies have demonstrated a variety of collective behaviors in such systems, including jamming and crystallization in light-responsive robot swarms,[20,21] disorder-to-order transitions induced by spontaneous cooling regulation,[22] adaptive locomotion and self-reconfiguration in robotic metamaterials,[23,24] and chiral motion and hyperuniformity in multispecies robot collectives with non-reciprocal alignment interactions.[25] At the microscopic scale, feedback-controlled colloidal systems naturally access fluidic conditions relevant to microorganisms and cells and can be scaled up to large ensembles with relatively low hardware costs. Under structured illumination, colloidal particles can be driven by local temperature or concentration gradients, and real-time feedback further endows them with effective sensing and information-processing

[†]Corresponding author. E-mail: Hepeng_zhang@sjtu.edu.cn

© 2026 Chinese Physical Society and IOP Publishing Ltd. All rights, including for text and data mining, AI training, and similar technologies, are reserved.

capabilities.[8,26–34] Such platforms have enabled studies of quorum sensing,[27] perception-dependent mobility,[8] vortex formation,[28,30] Vicsek-type dynamics,[31] physical reservoir computing,[32] time-delay dynamics,[33] and swarm control through counterfactual reinforcement learning.[34] However, microscopic colloidal systems are often subject to stronger stochastic fluctuations, and short-range couplings in the fluid environment can be difficult to isolate and quantify.

Here, we introduce a feedback-controlled optoelectronic tweezers (OET) platform, in which patterned illumination on an a-Si:H photoconductive electrode generates reconfigurable electric fields and dielectrophoretic forces at ultralow optical intensities. The platform retains the microscale, low-Reynolds-number physical environment of colloidal active matter while enabling low-disturbance and quantitatively controlled programming of both single-particle motility and interparticle interactions. Although OET has previously been integrated with robotic algorithms for real-time path planning and collision avoidance of biological targets,[35] its use as a programmable physical environment for engineering active-matter interactions remains largely unexplored. We therefore first quantitatively calibrate single-particle motility, control uncertainty, and dipolar electrostatic interactions, thereby establishing a minimal and transparent physical environment. Building on this calibrated baseline, we realize active Brownian particles (ABPs) with independently tunable motility parameters and programmable interaction rules. As a second demonstration, we implement chemotactic-field-mediated interactions between active particles, enabling their self-assembly into edge-dense, center-symmetric structures.

2. Feedback-controlled optoelectronic platform

Our experimental setup is schematically illustrated in Fig. 1(a). Polymethyl methacrylate (PMMA) microspheres of radius $a = 5$ μm are confined in an opto-electronic tweezer (OET) chip and actuated by individually addressed blue-light spots (450 nm wavelength). The illumination patterns are generated by a spatial light modulator (SLM) and projected onto the chip through a 10× objective. Particle motion is recorded by a digital camera through a 4× objective under uniform red illumination (660 nm wavelength), and the particle positions are tracked in real time. The detected positions are streamed to the computer, which computes the required updates and drives the SLM to continuously adjust the locations and intensities of the light spots. In this closed-loop configuration, both the magnitude and direction of the DEP force acting on each particle can be prescribed in real time, enabling fully programmable two-dimensional control of particle motion.

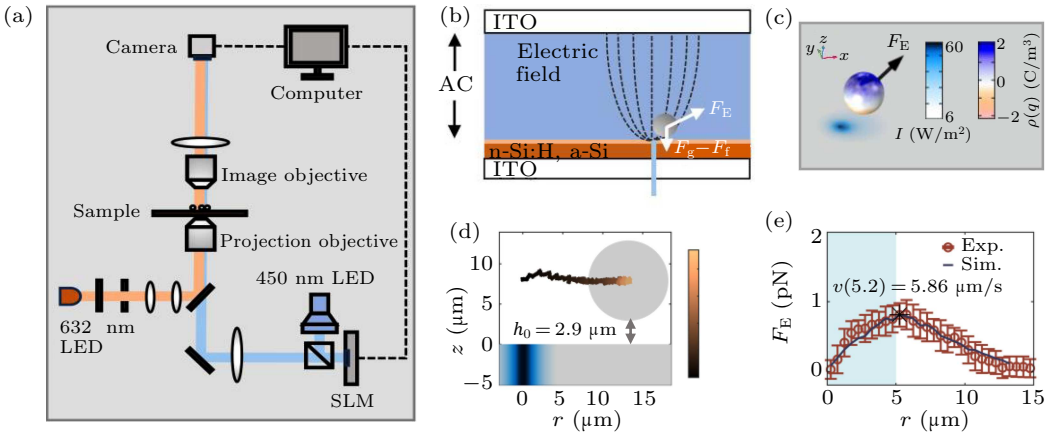


Fig. 1. Experimental setup and actuation mechanism. (a) Schematic of the feedback-controlled optoelectronic tweezer (OET) platform. (b) OET chip geometry and force components acting on a particle near a blue-light spot. The electrode gap H is 100 μm; an AC voltage of 20 V_{pp} at 300 kHz is applied. (c) Finite-element calculation of the induced charge density and the resulting dielectrophoretic (DEP) force near a circular blue-light spot. (d) Experimental three-dimensional particle trajectory measured by holographic microscopy; the equilibrium levitation height without blue light spot is $h_0 = 2.9$ μm. The blue shaded area indicates the projected light spot. (e) Variation of the mean radial DEP force $F_E(r)$ with the lateral spot–particle distance. The blue line shows numerical results. The Gaussian blue-light spot has a full width at half maximum (FWHM) of 4.7 μm and a peak intensity of 6.06 mW/cm^2.

2.1. Actuation mechanism

The opto-electronic chip consists of upper and lower electrodes (Fig. 1(b)). The lower electrode is coated with hydrogenated amorphous silicon (a-Si:H),[36–38] enclosing a liquid film of thickness 100 μm. An AC voltage of 20 V_{pp} at 300 kHz is applied across the electrodes. Upon blue-light illumination, electron–hole pairs are generated within the a-Si:H layer, raising the local photoconductivity by up to four orders of magnitude compared to the dark state.[39] Because the photoconductive response of a-Si:H at 450 nm is more than two orders of magnitude stronger than at 660 nm,[40] blue light can efficiently reshape the electric-field distribution while red light can be used for imaging without perturbing particle motion. The light-induced increase in photoconductivity locally lowers the impedance of the a-Si:H layer in the illuminated region, generating a steep conductivity gradient that produces

a strongly nonuniform electric field in the surrounding liquid. Because the conductivity and permittivity of the microspheres differ from those of the medium, each sphere becomes polarized in this field (with the induced charge density illustrated in Fig. 1(c)). The polarized particles then experience negative dielectrophoresis in the nonuniform field and are driven away from the illuminated region in our experiments.[41,42]

In the low-Reynolds-number regime near a wall, the particle velocity $\boldsymbol{v}$ in the horizontal plane is linearly related to the DEP force F_{E} according to[43]

$$\boldsymbol{v} = \mu(h)\boldsymbol{F}_{\mathrm{E}}, \tag{1}$$

where $\mu(h)$ is a height-dependent mobility and h denotes the separation between the particle and the wall. Using finite-element Stokes-flow calculations under the experimental geometry, we determine $\mu(h)$ for a particle at different heights h above the bottom plate, as shown in Fig. S12 in the supplementary information. We actuate a particle by projecting a Gaussian blue-light spot beneath it. The three-dimensional particle trajectory is measured using digital holographic microscopy and plotted in Fig. 1(d). The particle is propelled predominantly in the horizontal plane away from the light spot, while exhibiting a weak vertical displacement (typically < 1 μm), indicating quasi-two-dimensional motion. We use Eq. (1) to compute the radial dielectrophoretic force $F_{\mathrm{E}}(r)$ from the particle velocity and plot the averaged result from 40 independently tracked particles as symbols in Fig. 1(e). The DEP force peaks when the spot is positioned near the particle surface ($r = a$) and decays rapidly over a distance of $3a$, defining the effective range of opto-electronic actuation. This spatial dependence is also investigated by finite-element calculations that resolve the light-induced electric field and compute the corresponding DEP force through the Maxwell stress tensor (Section 2 in the supplementary information). We evaluate the DEP force acting on a particle positioned along the experimentally measured trajectory; numerical results (solid line in Fig. 1(e)) are in good agreement with experimental values. At a distance $r = 5.2$ μm, the particle velocity is $v_{\mathrm{E}}(r = 5.2\ \mu\mathrm{m}) = 5.86$ μm/s, corresponding to a DEP force $F_{\mathrm{E}}(r = 5.2\ \mu\mathrm{m}) = 0.65$ pN.

2.2. Feedback-programmed single-particle motility

After characterizing the particle motion induced by a spatially fixed light spot, we next employ the feedback mechanism to move the spot synchronously with the particle, thereby achieving continuous and programmable driving. At time t, particle i is detected at position $\boldsymbol{r}_{i,t}$. A Gaussian blue-light spot of intensity $I_{i,t}$ is then positioned near the particle at $\boldsymbol{X}_{i,t} = \boldsymbol{r}_{i,t} - d_l(\cos\Theta_{i,t}, \sin\Theta_{i,t})$, where $\Theta_{i,t}$ specifies the programmed driving direction. We choose a fixed offset $d_l = 5$ μm, corresponding to placing the light spot near the particle rim, which maximizes the propulsion speed while keeping vertical motion small (Fig. 1(d)). The resulting DEP force drives the particle with an instantaneous speed $v_{i,t}$ along direction $\Theta_{i,t}$. A detailed discussion on the feedback control mechanism can be found in Sections 1.E and 1.F in the Supporting Information.

To prescribe particle motion, we establish a calibration function $I_{i,t} = \mathcal{F}(F_{E,i,t})$ which maps a target DEP force to the required light intensity. The function $\mathcal{F}$ is obtained experimentally by driving a group of particles with light spots of fixed direction Θ and constant intensity I. Representative trajectories are shown in the inset of Fig. 2(a). Instantaneous speeds are computed using forward differencing $v(t) = |\boldsymbol{x}(t+\Delta t) - \boldsymbol{x}(t)|/\Delta t$, where Δt is the feedback interval. For each light intensity, particle motions are decomposed into components parallel $v_{\parallel}$ and perpendicular $v_{\perp}$ to the spot–particle axis. As shown in Fig. 2(a), both components follow Gaussian statistics[29]

$$p(v_{\parallel}) \propto \exp\left[-\frac{(v_{\parallel} - \bar{v}_{\parallel})^2}{2\varepsilon_{\parallel}^2}\right],$$
$$p(v_{\perp}) \propto \exp\left[-\frac{(v_{\perp} - \bar{v}_{\perp})^2}{2\varepsilon_{\perp}^2}\right]. \tag{2}$$

The mean values $\bar{v}_{\parallel}/\bar{v}_{\perp}$ and standard deviations $\varepsilon_{\parallel}/\varepsilon_{\perp}$ characterize the response and fluctuations of the particle motion for a given illumination intensity. Using the independently determined height-dependent mobility $\mu(h_0)$, these measured velocities are converted into the corresponding effective DEP forces (Eq. (1)), yielding a calibration between illumination intensity and driving force (Fig. 2(b)). The resulting calibration curve is well described by a double-exponential form, $\mathcal{F}(F_{\mathrm{E}}) = \alpha_1 \mathrm{e}^{\alpha_2 F_{\mathrm{E}}} + \alpha_3 \mathrm{e}^{\alpha_4 F_{\mathrm{E}}}$. The calibrated DEP force depends on the dielectric contrast between the particles and the surrounding medium, and therefore on the effective Clausius–Mossotti response under the applied AC field. Changes in the medium conductivity can alter this polarization response and hence the DEP-force magnitude. Temperature variations may further affect both the dielectric properties and the fluid viscosity, thereby modifying the force calibration and the resulting particle mobility. This calibration is repeated at the beginning of each experiment to account for variations in illumination conditions, the photoconductive response of the OET substrate, and changes in the conductivity or temperature of the liquid medium.

Using the calibration function $I_{i,t} = \mathcal{F}(F_{E,i,t})$, we dynamically adjust the illumination intensity to prescribe a time-dependent driving DEP force on the particle, which results in a velocity by Eq. (1) for an isolated particle. This capability is shown in Movie S1. We impose a sinusoidally modulated driving force corresponding to a nominal velocity profile $\boldsymbol{v}(t) = 15\sin(\pi t/10)\hat{\boldsymbol{e}}_{\Theta}$ μm/s along a fixed direction. As shown in Fig. 2(c) and Movie S1, the measured velocity matches closely with the prescribed profile, demonstrating robust and precise control over time-dependent driving.

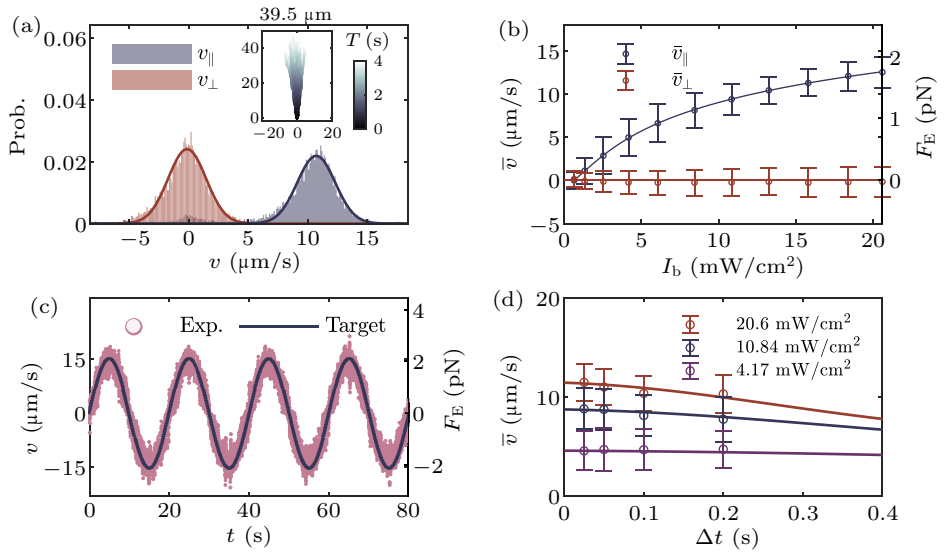


Fig. 2. Feedback-controlled single-particle dynamics. (a) Probability density functions of the velocity components parallel ($v_\parallel$) and perpendicular ($v_\perp$) to the spot–particle axis, with Gaussian fits. Inset: trajectories of 40 particles driven at constant DEP force. (b) Mean particle speed $v_{\parallel/\perp}$ and standard deviations $\varepsilon_{\parallel/\perp}$ versus light intensity I_b (left axis). The right axis shows the corresponding driving force F_E, obtained using the height-dependent mobility $\mu(h_0)$ and Eq. (1). The blue solid line is a fit to $\mathcal{F}(F_E) = \alpha_1 e^{\alpha_2 F_E} + \alpha_3 e^{\alpha_4 F_E}$. (c) Prescribed time-dependent target velocity $v(t) = 15\sin(\pi t/10)$ and measured particle velocity. The corresponding driving force F_E is shown on the right axis. (d) Mean particle velocity versus feedback interval Δt. The solid line shows the model prediction based on the radial velocity profile $F_E(r) \sim e^{-(r-b_1)^2/b_2^2}$ with $b_1 = 5.5$ μm and $b_2 = 4.5$ μm.

Feedback interval Δt is a crucial parameter that determines the accuracy of our control strategy. To demonstrate its effect, we drive particles along a fixed direction using different feedback intervals Δt under three illumination intensities. As shown in Fig. 2(d), the measured particle velocity $\bar{v}$ decreases with increasing Δt, with the effect being more pronounced at higher light intensities, corresponding to faster target speeds. This observation can be understood as follows. During each feedback cycle, the light spot remains fixed while the particle continues to move, leading to an increasing separation between the particle and the light spot and a concomitant reduction of the DEP propulsion force. As a result, the time-averaged particle velocity over one feedback interval,

$$\bar{v} = \frac{1}{\Delta t}\int_t^{t+\Delta t} v_E(r(t'))\,dt', \tag{3}$$

decreases for longer Δt or higher propulsion velocity. By incorporating the phenomenological fit of the radial velocity profile, $v_E(r) \sim \exp[-(r-b_1)^2/b_2^2]$ (fitting result illustrated in Fig. S8) into the feedback model, we predict a monotonic decrease of the mean particle speed with increasing feedback interval Δt (Fig. 2(d)), which is confirmed by experimental measurements. A second timescale that influences control performance is the latency between image acquisition and light-spot projection, during which image processing and light-pattern generation are performed. As discussed in Section I.F of the supplementary information, this latency primarily affects the magnitude of velocity fluctuations. To ensure reliable control accuracy in the experiments, we choose a feedback interval of $\Delta t = 0.025$ s and restrict the prescribed DEP force to values below a saturation force of $v_m/\mu(h)$, where saturation speed is $v_m = 7.5$ μm/s.

2.3. Particle–particle Interactions

In our system, AC-induced polarization gives rise to long-range dipolar electrostatic repulsion between particles,[44,45] while particle motion generates Stokes flows that hydrodynamically entrain nearby particles.[43,46] These electrostatic and hydrodynamic couplings constitute the intrinsic interaction channels that define the baseline interaction landscape of the system.

To extract the electrostatic interaction law, we drive two well-separated particles toward each other using equal inward DEP forces F_E. At large separations, electrostatic repulsion is negligible and the particles approach each other at a constant speed $v_0 = \mu(h)F_E$. As the interparticle separation decreases, the repulsive interaction grows and progressively slows the approach. The particles eventually reach an equilibrium separation r_0, at which the outward electrostatic force F_D balances the inward DEP force F_E (Fig. 3(a)). By varying F_E and measuring the corresponding equilibrium distance r_0, we directly extract the electrostatic force law. The experimental results, together with finite-element calculations, are shown in Fig. 3(a). We find that the electrostatic force obeys the scaling $F_D \propto r_0^{-4}$, consistent with induced dipole–dipole repulsion,[44]

$$\boldsymbol{F}_D(r_{ij}) = \frac{K_e a^6}{\mu(h_0)\, r_{ij}^4}\,\hat{\boldsymbol{r}}_{ij}, \tag{4}$$

where r_{ij} is the center-to-center separation between particles i and j, $\hat{\boldsymbol{r}}_{ij}$ is the corresponding unit vector, and the interaction

strength $K_e \approx 3.96 \times 10^7\ (\mathrm{m \cdot s})^{-1}$ is obtained from fits to the experimental and numerical data.

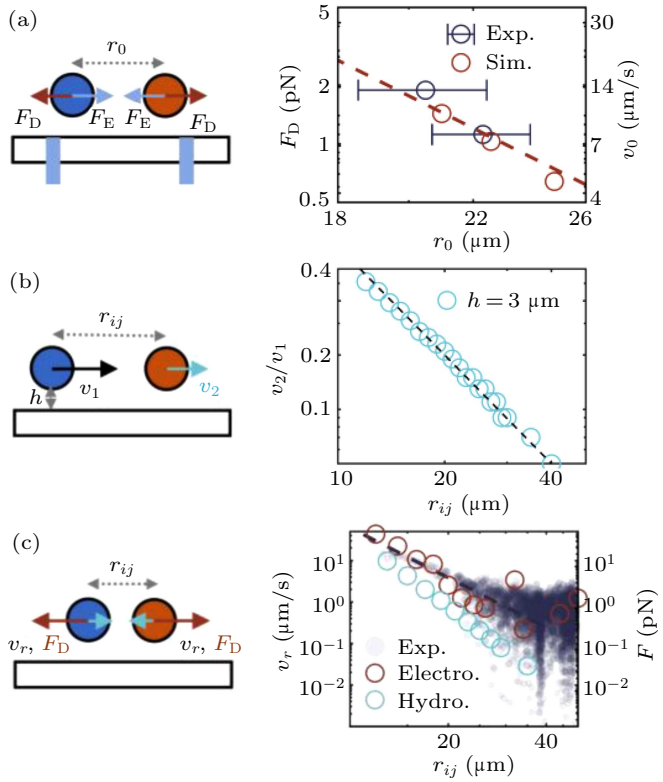


Fig. 3. Electrostatic and hydrodynamic pair interactions. (a) Two particles driven toward each other by feedback-controlled light spots reach force equilibrium at separation r_0. Symbols show the measured approach speed v_0 (blue) and the calculated electrostatic force F_D (red) at equilibrium, yielding $F_D \propto r_0^{-4}$ (dashed line). (b) Hydrodynamic entrainment. A particle driven at $v_1 = 5$ μm/s induces a velocity v_2 on a neighboring particle at distance r_{ij}, as obtained from finite-element Stokes-flow calculations, with $v_2/v_1 \propto r_{ij}^{-2}$ (dashed line) at $h = 3$ μm. (c) Experimental radial separation velocity v_r of nearby particles (gray dots), resulting from combined electrostatic and hydrodynamic interactions and scaling as $v_r \propto r_{ij}^{-4}$ (dashed line). Blue and red circles show the corresponding hydrodynamic entrainment velocity and electrostatic force evaluated at the measured r_{ij} and v_r.

Hydrodynamic interactions are investigated using finite-element Stokes-flow simulations. As illustrated in Fig. 3(b), two particles are positioned at the same height h above the electrode and separated by a distance r_{ij}. The left particle is driven at a prescribed horizontal velocity $v_1 = 5$ μm/s. The entrainment velocity v_2 is defined as the velocity at which the net hydrodynamic force on the right particle vanishes, thereby providing a direct measure of the hydrodynamic coupling. Repeating this procedure for different separations r_{ij} at a fixed height $h = 3$ μm yields the distance dependence of the hydrodynamic interaction. As shown in Fig. 3(b), the induced velocity decays as

$$v_2 = \frac{K_h v_1}{r_{ij}^2}, \tag{5}$$

where $K_h = 7.8 \times 10^{-11}$ m^2 characterizes the coupling strength and is obtained by fitting the numerical results.

The electrostatic and hydrodynamic interaction laws are further tested in independent experiments. We first turn off the voltage applied to the electrodes, identify two nearby particles, and then reapply the voltage without imposing any illumination pattern. The resulting electrostatic repulsion drives the particles apart, and the radial separation velocity decays as $v_r \propto r_{ij}^{-4}$, as shown by the gray symbols in Fig. 3(c). Using Eq. (4), we estimate the electrostatic force F_D and the corresponding velocity contribution $\mu(h)F_D$ at each separation. The predicted velocities are in good agreement with the experimental measurements. By contrast, the hydrodynamic contribution computed from Eq. (5) is substantially smaller over the separation range probed here, showing that electrostatic dipolar repulsion provides the leading contribution to the measured radial separation dynamics. Nevertheless, when particles are very close, hydrodynamic entrainment can act as a near-field correction and slightly modify the relative velocity. Accordingly, the close-range pair dynamics should be interpreted as primarily electrostatic, with an additional weaker hydrodynamic contribution.

3. Experimental realizations of programmable active matter

Our actuation and control framework naturally extends from single-particle manipulation to programmable many-body organization. In the following, we demonstrate two representative realizations enabled by the platform: an experimental implementation of the standard active Brownian particle (ABP) model with independently tunable motility parameters, and programmable self-assembly of communicating active particles.

3.1. Feedback-controlled colloids as an experimental ABP realization

Over the past two decades, the ABP model has become a standard minimal description of active matter, in which particles undergo constant self-propulsion with orientational persistence and rotational noise. This simple framework captures a wide range of nonequilibrium phenomena, including collective motion and motility-induced phase separation (MIPS)[3,4,47–50] and has therefore become central to the study of nonequilibrium phase coexistence, interfacial behavior, and the breakdown of equilibrium intuition in active systems.[47,51] However, in experiments it is challenging to independently tune the propulsion speed, rotational diffusion, and interparticle interactions.[11,52–55]

Motivated by these challenges, we use our platform to realize a minimal ABP system, whose target dynamics are prescribed as

$$\dot{\boldsymbol{r}}_i = v_0 \boldsymbol{n}_i, \quad \dot{\theta}_i = \sqrt{2D_r}\,\eta_i(t), \tag{6}$$

where v_0 is the propulsion speed, $\boldsymbol{n}_i = (\cos\theta_i, \sin\theta_i)$ denotes the particle polarity, and D_r is the effective rotational diffusion coefficient of the realized ABP dynamics. Here, $\eta_i(t)$

is Gaussian white noise with $\langle \eta_i(t) \rangle = 0$ and $\langle \eta_i(t)\eta_j(t') \rangle = \delta_{ij}\delta(t-t')$. Translational Brownian diffusion is neglected due to the large particle size.

Experimentally, these dynamics are implemented using feedback-controlled light spots with intensity $I_\mathrm{b} = 1.83\ \mathrm{mW/cm^2}$. For each particle, a light spot is placed at a fixed distance from the particle center with fixed intensity, so that the resulting DEP generates self-propulsion with speed v_0. The instantaneous propulsion direction is determined by the vector from the particle center to its assigned light spot. To introduce orientational fluctuations, we let the angular position Θ_i of the light spot relative to the particle evolve stochastically according to

$$\Theta_i(t+\Delta t) = \Theta_i(t) + \Delta\Theta_i, \tag{7}$$

where $\Delta\Theta_i$ is sampled from a Gaussian distribution $\Delta\Theta_i \sim \mathcal{N}(0, 2D_\Theta \Delta t)$ generated by a standard pseudorandom number generator. Through this stochastic update of the spot direction, the particle realizes ABP-like motion, and the corresponding effective rotational diffusion coefficient D_r is quantified below from the measured trajectories by fitting the MSD.

We measure particle trajectories in a dilute suspension with an area fraction below 0.15% (inset of Fig. 4(a)) and compute the mean-squared displacement (MSD). As shown in Fig. 4(a), the MSD exhibits ballistic scaling at short times, $\mathrm{MSD} \sim t^2$, and crosses over to diffusive behavior at long times, $\mathrm{MSD} \sim t$.[4,47] We fit the measured MSD to the standard free-ABP prediction[4,47]

$$\langle \Delta r^2(t) \rangle = \frac{2v_0^2}{D_\mathrm{r}^2}\left(D_\mathrm{r}t + \mathrm{e}^{-D_\mathrm{r}t} - 1\right), \tag{8}$$

from which we extract the propulsion speed v_0 and the rotational diffusion coefficient D_r. In this analysis we neglect translational Brownian diffusion, which is subdominant on the timescales and length scales probed here. As shown in Figs. 4(b) and 4(c), the fitted parameters quantitatively confirm the programmability of ABP motility in our platform.

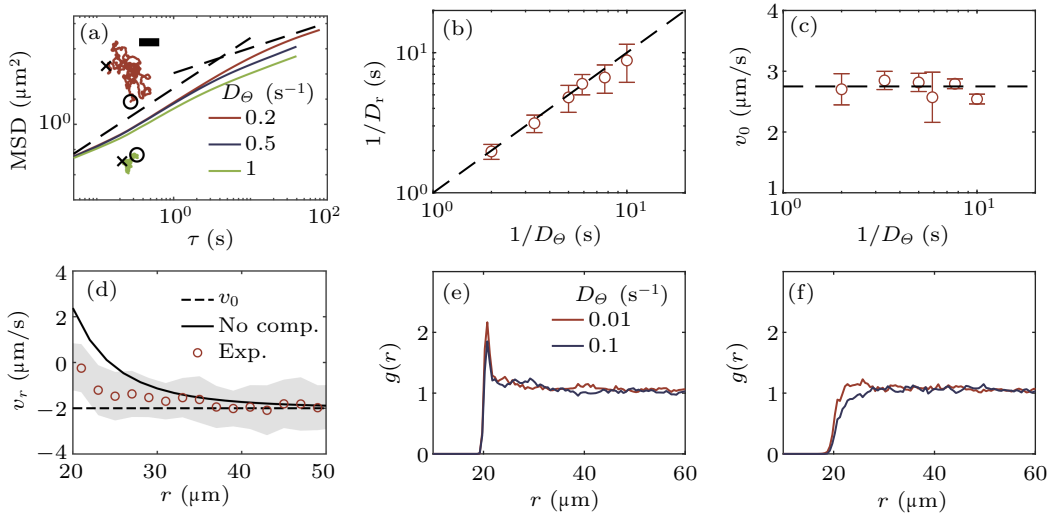


Fig. 4. Feedback-controlled realization of active Brownian particles (ABPs). (a) Mean-squared displacement (MSD) for particles under different prescribed angular-noise strengths D_Θ. Dashed lines indicate short-time ballistic scaling $\sim \tau^2$ and long-time diffusive scaling $\sim \tau$. Insets show representative trajectories for $D_\Theta = 0.2\ \mathrm{s^{-1}}$ (red) and $1\ \mathrm{s^{-1}}$ (cyan). (b) Measured orientational persistence time $(1/D_\mathrm{r})$ versus the prescribed noise timescale $(1/D_\Theta)$; the dashed line indicates $1/D_\mathrm{r} = 1/D_\Theta$. (c) Measured propulsion speed v_0 versus the prescribed noise timescale $(1/D_\Theta)$; the dashed line denotes the mean speed. (d) Velocity of two approaching particles when dipolar repulsions are compensated by feedback control (see text). The solid line shows the estimated velocity in the absence of compensation. (e) Pair correlation function $g(r)$ for low-density ABPs with compensated dipolar repulsions. (f) Pair correlation function $g(r)$ for low-density ABPs with uncompensated dipolar repulsions.

Having validated the single-particle dynamics in the dilute limit, where interactions are negligible, we next extend the feedback scheme to program interparticle interactions. The same closed-loop architecture allows us to superimpose an arbitrary, user-defined interaction model on top of the prescribed propulsion. Specifically, the overdamped Langevin dynamics of particle i reads

$$\begin{aligned} \dot{\boldsymbol{r}}_i &= v_0\boldsymbol{n}_i + \mu(h_0)\sum_{j\neq i}\boldsymbol{F}^{\mathrm{prog}}(\boldsymbol{r}_{ij}) + \mu(h_0)\sum_{j\neq i}\boldsymbol{F}_\mathrm{D}(\boldsymbol{r}_{ij}), \\ \dot{\theta}_i &= \sqrt{2D_\mathrm{r}}\,\eta_i(t), \end{aligned} \tag{9}$$

where $v_0\boldsymbol{n}_i$ sets the target propulsion, $\boldsymbol{F}^{\mathrm{prog}}(\boldsymbol{r}_{ij})$ is a programmable pairwise force that can encode an arbitrary interaction rule, and $\boldsymbol{F}_\mathrm{D}(\boldsymbol{r}_{ij})$ denotes the electrostatic dipolar repulsion of the physical particles (Eq. (4)). Experimentally, both the propulsion and the programmed interaction are realized by the feedback controller through the placement of illumination spots and the modulation of their intensities. As a demonstration, we design $\boldsymbol{F}^{\mathrm{prog}}$ to compensate the dipolar repulsion while preserving a strong short-range exclusion:

$$\mu(h_0)\boldsymbol{F}^{\mathrm{prog}}(\boldsymbol{r}_{ij}) = \begin{cases} v_m\hat{\boldsymbol{r}}_{ij} - \dfrac{K_a a^6}{|\boldsymbol{r}_{ij}|^4}\hat{\boldsymbol{r}}_{ij}, & |\boldsymbol{r}_{ij}| \le 2r_\mathrm{c}, \\ -\dfrac{K_a a^6}{|\boldsymbol{r}_{ij}|^4}\hat{\boldsymbol{r}}_{ij}, & |\boldsymbol{r}_{ij}| > 2r_\mathrm{c}, \end{cases} \tag{10}$$

where $\boldsymbol{r}_{ij} = \boldsymbol{r}_i - \boldsymbol{r}_j$ and $\hat{\boldsymbol{r}}_{ij} = \boldsymbol{r}_{ij}/|\boldsymbol{r}_{ij}|$. Here, $v_{\mathrm{m}} = 8$ μm/s sets the magnitude of a constant outward drift that enforces a hard exclusion for separations $|\boldsymbol{r}_{ij}| \le 2r_{\mathrm{c}}$, with $r_{\mathrm{c}} = 10$ μm. The coefficient $K_{\mathrm{a}} = 3.9 \times 10^7\ (\mathrm{m}\cdot\mathrm{s})^{-1}$ is chosen such that the long-ranged term in Eq. (10) compensates the drift generated by the electrostatic dipolar repulsion as defined in Eq. (4).

To quantify the resulting effective interaction, we consider a two-particle experiment in which two particles are driven to move toward each other with prescribed speed v_0 along their line of centers. With the compensation enabled, the measured relative approach speed v_r remains close to v_0 for $r > 2r_{\mathrm{c}}$ and then rapidly decreases to zero as $r \to 2r_{\mathrm{c}}$, as shown by symbols in Fig. 4(d). For comparison, the approach speed expected in the absence of compensation is plotted as the black solid line, $\mu(h_0)F^{\mathrm{D}}(r) - v_0$. Overall, the compensation scheme yields an effective hard-disk-like interaction: particles approach nearly freely down to $r \simeq 2r_{\mathrm{c}}$, where the imposed short-range exclusion arrests further approach, corresponding to an effective disk radius r_{c}.

We quantify the collective consequences of the programmed interactions by measuring the pair correlation function $g(r)$ in many-particle systems with and without compensation. Experiments are performed with $N = 200$ ABPs in a square arena of size $L = 1000$ μm with reflecting boundaries (see Movie S2 and supplementary information Section 4). With compensation enabled, $g(r)$ displays a pronounced peak near $r \simeq 2r_{\mathrm{c}}$ together with a sharp exclusion for $r < 2r_{\mathrm{c}}$, consistent with effective hard-disk-like interactions (Fig. 4(e)). In contrast, without compensation, $g(r)$ increases smoothly beyond the excluded separation set by the maximal active drift and shows no pronounced peak, consistent with a long-range dipolar repulsion (Fig. 4(f)).

Looking ahead, this tunability provides a practical route to test whether long-ranged hydrodynamic and/or electrostatic interactions obscure MIPS in active-matter experiments.[56] In particular, by increasing the exclusion distance r_{c} while keeping the single-particle motility fixed, we can suppress the relative contribution of long-ranged interactions and drive the system toward an effectively short-ranged, purely repulsive ABP limit.

3.2. Interaction and assembly of communicating active particles

Many biological and synthetic agents navigate by producing (or consuming) a shared scalar "resource" field and adjusting their motion according to the deviation of the locally sensed field from an individually preferred optimum. To investigate this interesting phenomenon, we use our platform to implement the communicating active-particle model of Ref. [57]. In this model, the field $c(\boldsymbol{r},t)$ (e.g., oxygen, chemoattractant, or temperature) evolves according to a diffusion–decay equation with point sources at the particle positions and, in the fast-field (adiabatic) limit, yields a quasistatic superposition of Yukawa kernels,

$$c(\boldsymbol{r}) = \sum_j Y(|\boldsymbol{r} - \boldsymbol{r}_j|),$$
$$Y(r) = A\frac{\mathrm{e}^{-\kappa r}}{r}, \quad \kappa = \sqrt{k_{\mathrm{d}}/D}, \tag{11}$$

where D and k_{d} are the diffusion coefficient and decay rate of the field $c(\boldsymbol{r},t)$. Each agent then moves either up or down the local gradient depending on whether the sensed field is below or above the optimal value c_{op}, as encoded by

$$\boldsymbol{F}_i = -\lambda\left(c(\boldsymbol{r}_i) - c_{\mathrm{op}}\right)\nabla_i c(\boldsymbol{r}_i). \tag{12}$$

Substituting Eq. (11) into Eq. (12) makes explicit that the resulting interactions are generically non-pairwise: the force can be decomposed as $\boldsymbol{F}_i = \boldsymbol{F}_{i,\mathrm{p}} + \boldsymbol{F}_{i,\mathrm{t}}$, where the Hamiltonian pair contribution reads

$$\boldsymbol{F}_{i,p} = -\lambda/2\nabla_i \sum_{j!=i}[Y(r_{ij}) - c_{\mathrm{op}}]^2, \tag{13}$$

and the intrinsically non-Hamiltonian triplet term is

$$\boldsymbol{F}_{i,t} = -\lambda\nabla_i \sum_{j\neq i}\sum_{\ell\neq i,\ \ell>j} Y(r_{ij})Y(r_{i\ell}), \tag{14}$$

highlighting the existence of effective three-body couplings beyond standard attraction–repulsion models. Interaction laws are incorporated into an overdamped Langevin equation to drive particle motion, defining a closed minimal model for collective self-optimization through field-mediated communication.[57]

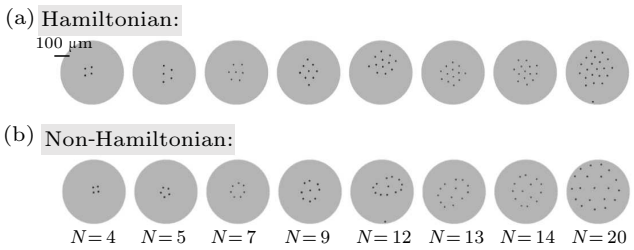


Fig. 5. Representative experimental snapshots of feedback-controlled assemblies with particle numbers $N = 4, 5, 7, 9, 12, 13, 14$, and 20. (a) Hamiltonian (pairwise) protocol. (b) Non-Hamiltonian protocol including triplet interactions. The corresponding control parameters are shown in Section 5 of the supplementary information.

We experimentally implement both the Hamiltonian (pairwise) protocol based on the pair term in Eq. (13) and the full non-Hamiltonian protocol including the triplet contribution in Eq. (14), using the same feedback-controlled architecture (see Movie S3). Experimental parameters and implementation details are provided in Section 5 of the supplementary information. We vary the particle number $N = 4$, 5, 7, 9, 12, 13, 14, and 20, and identify stable configurations after a relaxation time $T = 100$ s from random initial conditions (see Fig. 5). The Hamiltonian model yields ordered triangular-lattice clusters consistent with energy-minimizing

configurations of pairwise interactions (Eq. (13)), as shown by the top panels in Fig. 5. In contrast, in the non-Hamiltonian system, force balance can be achieved either by reaching the optimal field value, $c(\boldsymbol{r}_i) = c_{\rm op}$, or by forming locally uniform fields, $\nabla_i c(\boldsymbol{r}_i) = \mathbf{0}$ (Eq. (12)). The resulting assemblies (bottom panels in Fig. 5) are edge-dense and approximately center-symmetric, in agreement with the numerical findings of Ref. [57].

4. Discussion and conclusion

We have developed a feedback-controlled optoelectronic tweezers (OET) platform that enables programmable active colloids in a quasi-two-dimensional environment. In our platform, patterned illumination on an a-Si:H photoconductive electrode creates reconfigurable dielectrophoretic forces on particles (Fig. 1). We have calibrated the motility of individual particles and control uncertainty, and characterized dipolar electrostatic interactions between particles (Figs. 2 and 3). Building upon these measurements, we developed active Brownian particles with independently adjustable motility parameters and programmable interaction rules (Fig. 4). Additionally, we programmed communication-mediated interactions between the active particles, leading to self-assembly into edge-dense, center-symmetric structures (Fig. 5).

The scalability of the present platform is determined primarily by the duration of each feedback cycle and the time delay. While image acquisition and optical projection are approximately independent of particle number, the cost of particle tracking increases with system size, and the control computation depends on the interaction model being implemented (see Sections 1.E and 1.F in the Supporting Information). For pairwise programmable interactions evaluated explicitly over all particle pairs, the computational cost can approach $O(N^2)$, so the achievable feedback frequency decreases as the number of particles increases. Therefore, although the present platform already supports moderate-scale many-body experiments, further optimization of tracking and control algorithms will be important for larger-scale studies such as motility-induced phase separation. For the motility and interaction ranges explored here, the feedback delay, which is approximately 50 ms as analyzed in the Supporting Information, does not affect the main conclusions of the manuscript. For faster particles or larger many-body systems, however, predictive control strategies could further enhance the effective feedback bandwidth. In particular, state-estimation methods such as Kalman filtering may be used to predict particle positions in the next frame and partially compensate for processing delays, providing a promising route toward higher-speed and larger-scale active-matter experiments.

In our OET platform, each light spot functions as a switch that locally activates the electric field, enabling operation at very low optical intensities (1–100 $\mathrm{mW/cm^2}$). This low-intensity operation allows our platform to control large particle ensembles using a standard commercial LED source, significantly simplifying the generation of programmable light fields and facilitating scaling to large ensembles of particles. The dielectric response of the OET platform is governed by rapid Maxwell–Wagner relaxation,[37,44] occurring on the order of several microseconds, which leads to near-instantaneous generation of dielectrophoretic (DEP) forces in response to changes in illumination conditions. This rapid dielectric response supports robust real-time feedback control of DEP forces. The combination of low optical power requirements and fast dielectric response enables precise control over DEP forces acting on large ensembles of colloidal particles. These favorable characteristics make the OET platform particularly well-suited for investigating a wide range of active-matter phenomena, including non-reciprocal interactions and information-driven interaction rules. It also enables direct experimental testing of theoretical predictions and the development of adaptive materials based on programmable colloidal interactions.

Appendix A: Sample preparation and experimental setup

A dilute suspension of PMMA colloids (containing 0.01% Tween20, with a conductivity of approximately 40 $\mu\mathrm{S/cm}$ at 25 °C) is deposited onto the bottom plate of a chip. The top plate is then placed over the suspension, and the chip is sealed with adhesive tape around the edges. The electrode gap is 100 μm, and a 20 V_{pp}, 300 kHz AC voltage is applied across the plates.

The system is illuminated using a 660 nm light source with an intensity of approximately 0.15 $\mathrm{mW/cm^2}$ and imaged with a 4× objective (Nikon MRH20041) set to NA 0.13 and a camera (Basler acA2500-60um). Gaussian-shaped blue-light spots (450 nm) are projected onto the bottom surface to drive particle motion. Each spot has an intensity profile $I(r) = I_{\rm b}\exp(-r^2/2l_{\rm r}^2) + I_0$, where $l_{\rm r} = 2$ μm sets the characteristic length scale of the illumination and $I_0 = 0.64$ $\mathrm{mW/cm^2}$ accounts for a uniform background intensity arising from residual reflected light. These optical landscapes are generated using a spatial light modulator (HDSLM80Rplus) and relayed through a 10× objective (Nikon MRD00105) and a tube lens (Fig. 1(a)).

Appendix B: 3D trajectory reconstruction

We implement digital holographic microscopy by reducing the pinhole size in the red-light illumination path of Fig. 1(a). After calibrating the coordinate transformation between the imaging optics and the SLM, the objective lens is

defocused by approximately 100 μm above the microspheres. Once a particle is identified, a blue-light spot is projected at its center position, and images are recorded at 20 fps.

To reconstruct particle motion in three dimensions, we use HoloPy3.5 to generate forward holograms of a 5 μm-radius microsphere with refractive index $n_{\mathrm{p}} = 1.498$ under 660 nm illumination in an aqueous medium of refractive index $n_{\mathrm{m}} = 1.31$.[58] Synthetic holograms are compared to the measured intensity patterns, and the particle location (x, y, z) at each frame is obtained by fitting the hologram using the *cmaStrategy* of the HoloPy optimization routine. This procedure yields the time-resolved 3D trajectories of individual microspheres.

Acknowledgements

Discussions with Siyuan Yang and Yankai Xu are highly beneficial. HPZ acknowledges support from the National Natural Science Foundation of China (Grant Nos. 12225410 and 12074243) and the China Manned Space Engineering Program (Project number: KJZ-YY-NLT0502). SZ acknowledges support from the National Natural Science Foundation of China (Grant No. 62574023) and Chongqing Municipal Natural Science Foundation (Grant No. CSTB2024NSCQ-JQX0034).

References

[1] Ramaswamy S 2010 *Annu. Rev. Condens. Matter Phys.* **1** 323
[2] Vicsek T and Zafeiris A 2012 *Phys. Rep.* **517** 71
[3] Marchetti M C, Joanny J, Ramaswamy S, Liverpool T B, Prost J, Rao M and Simha R 2013 *Rev. Mod. Phys.* **85** 1143
[4] Bechinger C, Di Leonardo R, Löwen H, Reichhardt C, Volpe G and Volpe G 2016 *Rev. Mod. Phys.* **88** 045006
[5] Palacci J, Sacanna S, Steinberg A P, Pine D J and Chaikin P M 2013 *Science* **339** 936
[6] Yan J, Han M, Zhang J, Xu C, Luijten E and Granick S 2016 *Nat. Mater.* **15** 1095
[7] Morin A, Desreumaux N, Caussin J B and Bartolo D 2017 *Nat. Phys.* **13** 63
[8] Lavergne F A, Wendehenne H, Bäuerle T and Bechinger C 2019 *Science* **364** 70
[9] Liebchen B and Mukhopadhyay A K 2021 *J. Phys.: Condens. Matter* **34** 083002
[10] Gardi G and Sitti M 2023 *Phys. Rev. Lett.* **131** 058301
[11] Xu Y, Liu C, Liu J, Xu P, Xiao Z, Wang W and Zhang H P 2024 *Phys. Rev. Lett.* **133** 258304
[12] Karamouzas I, Skinner B and Guy S J 2014 *Phys. Rev. Lett.* **113** 238701
[13] Bastien R and Romanczuk P 2020 *Sci. Adv.* **6** eaay0792
[14] Cavagna A, Cimarelli A, Giardina I, Parisi G, Santagati R, Stefanini F and Viale M 2010 *Proc. Natl. Acad. Sci. USA* **107** 11865
[15] Dombrowski C, Cisneros L, Chatkaew S, Goldstein R E and Kessler J O 2004 *Phys. Rev. Lett.* **93** 098103
[16] Sokolov A, Aranson I S, Kessler J O and Goldstein R E 2007 *Phys. Rev. Lett.* **98** 158102
[17] Zhang H P, Be'er A, Florin E L and Swinney H L 2010 *Proc. Natl. Acad. Sci. USA* **107** 13626
[18] Chen C, Liu S, Shi X Q, Chaté H and Wu Y 2017 *Nature* **542** 210
[19] Volpe G, Bechinger C, Cichos F, *et al.* 2022 *npj Microgravity* **8** 54
[20] Wang G, Phan T V, Li S, Wombacher M, Peng C Q Y, Chen G, Goldman D I, Levin S A, Austin R H and Liu L 2021 *Phys. Rev. Lett.* **126** 108002
[21] Wang G, Phan T V, Li S, Wang J, Peng Y, Chen G, Qu J, Goldman D I, Levin S A, Pienta K, Amend S, Austin R H and Liu L 2022 *Proc. Natl. Acad. Sci. USA* **119** e2120019119
[22] Hou S X, Wang G, Ma X Y, Wang C Y, Wang P, Chen H C, Liu L Y and Wang J 2024 *Chin. Phys. B* **33** 078701
[23] Brandenbourger M, Locsin X, Lerner E and Coulais C 2019 *Nat. Commun.* **10** 4608
[24] Veenstra J, Scheibner C, Brandenbourger M, *et al.* 2025 *Nature* **639** 935
[25] Chen J, Lei X, Xiang Y, Duan M, Peng X and Zhang H P 2024 *Phys. Rev. Lett.* **132** 118301
[26] Khadka U, Holubec V, Yang H and Cichos F 2018 *Nat. Commun.* **9** 3864
[27] Bäuerle T, Fischer A, Speck T and Bechinger C 2018 *Nat. Commun.* **9** 3232
[28] Bäuerle T, Löffler R C and Bechinger C 2020 *Nat. Commun.* **11** 2547
[29] Fränzl M, Muiños-Landin S, Holubec V and Cichos F 2021 *ACS Nano* **15** 3434
[30] Wang X, Chen P C, Kroy K, Holubec V and Cichos F 2023 *Nat. Commun.* **14** 56
[31] Chen Z, Ding H, Kollipara P S, Li J and Zheng Y 2024 *Adv. Mater.* **36** 2304759
[32] Wang X and Cichos F 2024 *Nat. Commun.* **15** 774
[33] Chen Z and Zheng Y 2024 *Sci. Adv.* **10** eadk3914
[34] Heuthe V L, Panizon E, Gu H and Bechinger C 2024 *Sci. Robot.* **9** eado5888
[35] Liu J, Wang H, Liu M, Zhao R, Zhao Y, Sun T and Shi Q 2022 *Cyborg Bionic Syst.* **2022** 9890607
[36] Wu M C 2011 *Nat. Photonics* **5** 322
[37] Zhang S, Xu B, Elsayed M, Nan F, Liang W, Valley J K, Liu L, Huang Q, Wu M C and Wheeler A R 2022 *Chem. Soc. Rev.* **51** 9203
[38] Hong X, Xu B, Li G, Nan F, Wang X, Liang Q, Dong W, Dong W, Sun H, Zhang Y, Li C, Fu R, Wang Z, Wang G Y, Yao Y, Zhang S and Li J 2024 *Sci. Adv.* **10** eadn7582
[39] Chiou P Y, Ohta A T and Wu M C 2005 *Nature* **436** 370
[40] Liang W, Wang S, Dong Z, Lee G B and Li W 2012 *Micromachines* **3** 492
[41] Jones T B 1995 *Electromechanics of Particles* (Cambridge: Cambridge University Press)
[42] Liang S, Gan C, Dai Y, Zhang C, Bai X, Zhang B, Wheeler A R, Chen H and Feng L 2021 *Lab Chip* **21** 4379
[43] Happel J and Brenner H 1983 *Low Reynolds Number Hydrodynamics* (Dordrecht: Springer)
[44] Morgan H and Green N G 2003 *AC Electrokinetics: Colloids and Nanoparticles* (Baldock: Research Studies Press)
[45] Xu B, Ma Z, Fu R, Dong W, Li G, Li Z, Yang F, Hong X, Xie H, Huang C, Huang Y, Zhang X, Li H, Li J, Xie H, Tang J and Zhang S 2026 *Laser Photonics Rev.* **20** e01697
[46] Meiners J C and Quake S R 1999 *Phys. Rev. Lett.* **82** 2211
[47] Cates M E and Tailleur J 2015 *Annu. Rev. Condens. Matter Phys.* **6** 219
[48] Howse J R, Jones R A L, Ryan A J, Gough T, Vafabakhsh R and Golestanian R 2007 *Phys. Rev. Lett.* **99** 048102
[49] Volpe G and Gigan S 2014 *Sci. Rep.* **4** 3936
[50] Doostmohammadi A, Ignés-Mullol J, Yeomans J M and Sagués F 2018 *Nat. Commun.* **9** 3246
[51] Solon A and Zhao Y 2025 *Chin. Phys. Lett.* **42** 100901
[52] Elgeti J, Winkler R G and Gompper G 2015 *Rep. Prog. Phys.* **78** 056601
[53] Narinder N, Bechinger C and Gomez-Solano J R 2018 *Phys. Rev. Lett.* **121** 078003
[54] Karani H, Pradillo G E and Vlahovska P M 2019 *Phys. Rev. Lett.* **123** 208002
[55] Fernandez-Rodriguez I, Grillo F, Alvarez L, Rathlef M, Buttinoni I, Volpe G and Isa I 2020 *Nat. Commun.* **11** 4223
[56] Zhou T and Brady J F 2026 *Phys. Rev. Lett.* **136** 088301
[57] Zampetaki A V, Liebchen B, Ivlev A V and Löwen H 2021 *Proc. Natl. Acad. Sci. USA* **118** e2111142118
[58] Barkley S, Dimiduk T G, Fung J, Kaz D M, Manoharan V N, McGorty R, Perry R W and Wang A 2020 *Comput. Sci. Eng.* **22** 72